# Lifetime measurements with improved precision in $^{30,32}$S and possible influence of large-scale clustering on the appearance of strongly deformed states

P. Petkov,[1,2] C. Müller-Gatermann,[2] A. Dewald,[2] A. Blazhev,[2] C. Fransen,[2] J. Jolie,[2] P. Scholz,[2] K. O. Zell,[2] and A. Zilges[2]

[1] *"Horia Hulubei" National Institute for Physics and Nuclear Engineering R-76900 Bucharest-Măgurele, Romania*

[2] *Insitut für Kernphysik der Universität zu Köln, D-50937 Cologne, Germany*

(Received 5 May 2017; revised manuscript received 12 July 2017; published 26 September 2017)

The formation of large size clusters and/or their relative motion as possible excitation mode are suggested to be closely related to the origin of deformation in specific cases. In $^{32}$S, the consideration of some excitations in this nucleus as based on the existence of two doubly magic $^{16}$O clusters offers a possible solution to the long-standing problem of missing quadrupole collectivity in shell-model calculations aiming to describe electromagnetic $E2$ transition strengths and quadrupole moments. To experimentally check again this collectivity, lifetime measurements were performed on $^{30}$S and $^{32}$S. In $^{32}$S, at least, the reproduction of a number of observables supports the cluster scenario. Additionally, the superdeformed yrast band in $^{80}$Zr could find an explanation as based on the relative motion of two $^{40}$Ca clusters. Simultaneously, a necessity arises to revise experimentally some lifetimes derived in the past within the Blaugrund approximation when using the Doppler-shift attenuation method.

DOI: 10.1103/PhysRevC.96.034326

## I. INTRODUCTION

The nuclear many-body quantum problem involving basically two different kinds of particles, protons and neutrons, is not solved yet, due to reasons mainly related to the incomplete knowledge of the nuclear forces and the finite (but not small) number of nucleons $A$ characterizing most of the nuclei studied so far (see, e.g., Ref. [1]). The latter fact leads to a numerical treatment as the only possible solution, with applicability and precision strongly dependent on the computing power available (e.g., memory storage, computational speed). Nevertheless, relatively light nuclei, e.g., with $A \leqslant 40$, are already accessible to full shell-model calculations based on (nearly) first principles (a comprehensive review can be found in Ref. [2]). To perform such approximate calculations for heavier nuclei, the nucleons are grouped into closed shells (filled shells or core) and valence ones (i.e., occupying active orbitals above the filled shells) [3].

Another approach to treat the many-body problem is based on the consideration of the nucleus as composed from clusters, in the simplest case $\alpha$ particles. At the price paid for some phenomenology, this approach obviously reduces the number of considered constituents and has many experimental confirmations of its validity, especially in light nuclei [4]. Only relatively recently [5] have $\alpha$-cluster states been found in nuclei as heavy as $^{212}$Po, where an $\alpha$ particle is coupled to the doubly magic $^{208}$Pb core. These states decay via very strong $E1$ transitions because of the induced electric dipole moment in this mass-asymmetric composite system. More recently [6], states characterized by enhanced $E1$ strength of their decays have been interpreted within the framework of the *spdf* interacting boson model, providing further evidence for the formation of $\alpha$ clusters in medium-mass nuclei.

Larger clusters have been also observed (e.g., $^{12}$C), in most of the cases identified by exotic nuclear decays [7]. In the present work, we would like to address the question of whether large-scale clustering may participate in the generation of some collective motion at lower excitation energy close to the $0^+$ ground states of even-even nuclei. Therefore, we do not consider here properties normally related to giant resonances leading to phenomena associated with the formation of nuclear molecules [8]. As pointed out in Ref. [9], the $^{16}\mathrm{O} \times {}^{16}\mathrm{O}$ system is the most typical heavier cluster analog to the $\alpha \times \alpha$ cluster in $^{8}$Be. In that paper, it was shown that $^{16}\mathrm{O} \times {}^{16}\mathrm{O}$ cluster bands exist in $^{32}$S and their properties were derived using a unified description of bound and scattering states of the $^{16}\mathrm{O} \times {}^{16}\mathrm{O}$ system. Our intention is to check for possible influence of such bands on the structure of the lowest quadrupole excitations above the ground state in that nucleus.

In the present work, we will present more deeper considerations and improvements of the precision of the preliminary results published in Ref. [10], where the nucleus $^{32}$S was investigated in the context of large-size clustering. Moreover, we decided to reinvestigate experimentally the quadrupole collectivity in $^{30,32}$S, which up to our study pointed to a substantial enhancement unreproducible by the theoretical calculations available in the literature at present. Both shell-model [11–13] and mean-field (and beyond) (cf. Refs. [14,15] and references therein) approaches, when applied to the mass region, fail to describe such effects. For example, the multiparticle-multihole (mp-mh) configuration mixing (CM) treatment recently applied in Ref. [16] to 25 even-even $sd$-shell nuclei also indicated a lack of quadrupole collectivity in the model predictions.

Therefore, it seemed to us very important to check the empirical foundations of these conclusions by performing lifetime measurements, providing direct information on low-lying $B(E2)$ transition strengths, and more precisely on those of the $2_1^+ \rightarrow 0_1^+$ transitions. The point is that the progress in experimentation in past decades, from both instrumental and

 

data analysis points of view, could solve the problems that have hindered correct lifetime derivation in the past. Among these improvements, the most important are the higher efficiency of the multidetector arrays and the possibility to solve and/or minimize the side-feeding problems by using coincidences (e.g., $\gamma$-$\gamma$) and populating reactions with simpler mechanism, i.e., which do not involve complicated feeding patterns.

Experimentally, $^{32}$S was studied using different reactions and methods as tools aiming to the determination of specific properties (see, e.g., Refs. [17,18] and references therein). In particular, since this isotope is stable, it is accessible to Coulomb excitation experiments leading to the determination of $E2$ transition matrix elements as well as the quadrupole moment of the first excited $2^+$ state $Q = -15.4(2.0)\ e\,\mathrm{fm}^2$. Interestingly enough, the latter value is negative and large thus indicates a large prolate deformation as pointed out in Ref. [8]. The $B(E2; 2_1{}^+ \rightarrow 0_1{}^+)$ transition strength of about 10 W.u. [17] also suggests a considerable deformation in that relatively light ($A = 32$) nucleus. To newly investigate $^{32}$S, we used the $^{29}$Si($^4$He,$n$)$^{32}$S reaction at the vicinity of the Coulomb barrier ($V_C \propto 5.7$ MeV). In Ref. [17], a mean value of $\tau(2_1^+) = 244\,(16)$ fs was adopted by averaging the results of about 12 measurements. They are quite scattered, ranging from 175 to 360 fs, and therefore it is of significant interest to determine a reliable and precise value both for improving the experimental systematics and for providing a better basis for theoretical considerations.

Similar and even larger analog transition strength is observed in the neighboring $^{30}$S. In the latter case, the measurement of the $2_1{}^+$ lifetime using the Doppler-shift attenuation method (DSAM) technique, which yielded the longest result known so far, is presented in Ref. [19], where $\tau = 254\,(23)$ fs was determined. The average result in the National Nuclear Data Center (NNDC) database [20] is 225 (13) fs.

Since similar collectivity was found experimentally in many $A \approx 30$ nuclei (see Figs. 4(b) and 5 in Ref. [16] as well as discussion below), considerable theoretical efforts have been undertaken to reproduce those and other experimental data in that mass region. The numbers of protons and neutrons are being relatively small in the nuclei considered (about 14–18 for each species), and they do not represent an obstacle to advanced shell-model calculations and/or mp-mh configuration mixing. However, as already mentioned, the calculations arrive to theoretical $E2$ transition matrix elements and quadrupole moments of the $2_1{}^+$ levels which are insufficient to describe the larger collectivity of the corresponding experimental data. Thus, in Ref. [16], some theoretical $B(E2; 2_1{}^+ \rightarrow 0_1{}^+)$ values are only about 60% of the experimental ones, even after a renormalization leading to their maximal possible increase as for $^{30,32}$S. The theoretical quadrupole moments $Q(2_1{}^+)$ are also smaller, on average by 60%.

To address these problems, we decided to perform new lifetime measurements in $^{30,32}$S using DSAM and reactions which populate predominantly low-lying and more especially quadrupole states in these two nuclei. In the following, we will present the experiments, data analysis, and results and then turn our attention to the physical interpretation of the new data within the scope of the recent theoretical calculations discussed and some new ideas.

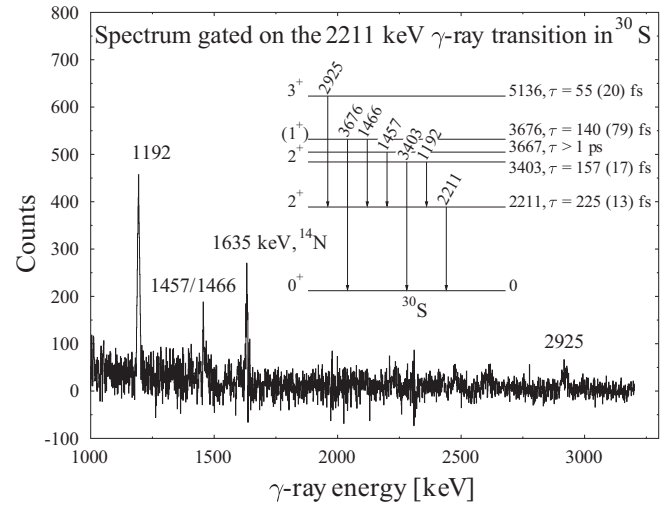


FIG. 1. Spectrum gated on the $2_1{}^+ \rightarrow 0_1{}^+$ transition in $^{30}$S using a matrix accumulating the statistics of all detectors (angles). A partial level scheme with data from Ref. [20] is also shown. The line of 1635 keV belongs to $^{14}$N obtained in a parasitic reaction on $^{12}$C. See also text.

## II. EXPERIMENTS

### A. Measurement for $^{30}$S

To investigate $^{30}$S, we used the $^{28}$Si($^3$He,$n$)$^{30}$S reaction at the vicinity of the Coulomb barrier using a beam energy of 8 MeV. Our experiment was performed at the FN Tandem of the University of Cologne, Germany. The target consisted of 1.0 mg/cm$^2$ natural Si deposited on 4.5 mg/cm$^2$ Ta foil. The $\gamma$ rays deexciting $^{30}$S were registered by the multidetector array Horus [21] in its specialized setup version described in Ref. [22]. Both singles and $\gamma$-$\gamma$ coincidences of different folds were collected for about one day. Among the 14 detectors of Horus, four pairs are suitable for Doppler-shift timing measurements being positioned at angles of 35, 45, 135, and 145 deg with respect to the beam axis. The coincidence data were sorted into matrices which were used to obtain pure gated spectra, allowing us to minimize the influence of the unknown (unobserved) feeding. It turned out that the statistics is not suffcient for a real coincidence analysis which eliminates the side feeding using the latter matrices. In Fig. 1, a spectrum obtained by gating on the $2_1{}^+ \rightarrow 0_1{}^+\gamma$-ray transition of 2211 keV is displayed. Using the partial level scheme in the insert, it is easy to identify the transitions feeding the $2_1{}^+$ level as well as the levels populated in the $^{28}$Si($^3$He,$n$)$^{30}$S reaction employed. This information can be compared with that obtained in the study [23] by Caraca *et al* ., namely with Fig. 1 in that work. There, the $^3$He beam energy was 6.5 MeV, i.e., a bit less than in the present work (8 MeV). At 6.5 MeV, only four states are populated, mainly directly as demonstrated by the time-of-flight (TOF) technique and coincidences with outgoing neutrons. These are the states at 2211, 3403, and 3667 keV as well as the ground state. The strongest direct population leads to the 3667-keV state. Of course, the higher lying states feed the lower lying ones by $\gamma$ decay. Obviously (see also the

singles $\gamma$-spectra analyzed below), at 8-MeV beam energy the situation is somewhat changed, with stronger direct population of the $2_1^+$ and then of the $2_2^+$ levels. Although small, a fusion-evaporation component in the reaction mechanisms is present. Since the energy balance restricts the excitation energy to about 5.5 MeV, and in that region the level density is extremely small, the contribution of the fusion-evaporation mechanism cannot be expected to play a very important role, but it should be taken into account in the analysis. In the following, on the basis of the above considerations supported by the information shown in Fig. 1, we shall treat the feeding of the $2_2^+$ level as exclusively direct. For the case of the $2_1^+$ level, we shall take into account both direct population at time $t = 0$ and the cascade feeding from upper levels, especially the $2_2^+$ one.

### B. Measurement for $^{32}$S

To investigate $^{32}$S, we used a $^4$He-induced reaction on $^{29}$Si with one outgoing neutron. The beam energy was 9 MeV, slightly higher compared to the Coulomb barrier than in the experiment for $^{30}$S.

This experiment was also performed at the FN Tandem of the University of Cologne, Germany. The target consisted of 0.5 mg/cm$^2$ $^{29}$Si on 5 mg/cm$^2$ Ta foil. The $\gamma$ rays deexciting $^{32}$S were registered by a setup normally used for plunger measurements. It consisted of 12 HPGe detectors positioned as follows with respect to the beam axis: (i) one detector at 0 deg considered as ring 0, (ii) six detectors at 45 deg (ring 1), and (iii) five detectors at 142.3 deg (ring 2). The distance between the target and the detectors was about 10 cm. It should be mentioned that the performance of some of the backward detectors deteriorated during the measurement and not all the data taken with them were considered in the offline analysis. Therefore, the final statistics accumulated at the backward angle was lower than that of ring 1. The coincidence data were sorted into matrices which were used to provide gated spectra with minimized influence of the unknown (unobserved) feeding. Differently from the $^{30}$S case, intense discrete feeders of the $2_1^+$ level were observed in addition to the direct population. This points to a modification of the relative weights of the two reaction mechanisms discussed above for $^{30}$S: direct transfer reaction and fusion evaporation. The details of the reasons for these changes are out of the scope of the present work. We note only that the increase of the beam energy and use of heavier projectiles are to some extent balanced by the larger negative $Q$ value of the reaction. It should be mentioned that without coincidences and different feeding paths the lifetime of the $2_1^+$ level would be impossible to measure in singles, with the $2_1^+ \rightarrow 0_1^+$ and $4_1^+ \rightarrow 2_1^+$ $\gamma$-ray transition energies differing only by a fraction of 1 keV. Being aware of this fact, we intentionally have chosen a slightly higher beam energy to ensure to the presence of feeders of the $2_1^+$ level.

## III. DATA ANALYSIS AND RESULTS

The lifetime determination in the framework of the Doppler-shift attenuation method (DSAM) is based on the time correlation between the slowdown of the recoiling ion and the decay of the nuclear level of interest (cf., e.g., Ref. [24]). The difference between the population patterns in the two experiments and the different states led to the use of two different variants for data analysis. A singles-like analysis with a single-exponential decay was performed in the case of predominant direct population proven by $\gamma$-$\gamma$ coincidences, i.e., when cascade feeding from higher lying states was not observed. This is the case of the the $2_2^+$ level in $^{30}$S and the states above the $2_1^+$ level in $^{32}$S. For the $2_1^+$ level in $^{30}$S, again a singles-like analysis was performed, but explicitly taking into account the feeding from the four populated higher lying states until about 5.5 MeV. For the $2_1^+$ level in $^{32}$S, gates on three different direct-feeding transitions could be set (gates from above, GFA) on shifted fractions of the line shapes of the feeders. The two procedures used are shortly presented below.

### A. Singles-like analysis

In the following, we shall denote by "singles-like analysis" procedures for analyzing DSAM data where no conditions for observation of other coincident $\gamma$-ray transitions are set or the gating conditions in coincidence matrices do not introduce modifications in the genuine time dependence of the decay of a given level. For example, the latter case can be associated with using wide gates covering the whole line shape, i.e., both shifted and unshifted components of the gating transition(s).

At a fixed direction of observation, e.g., at an angle $\theta$ with respect to the beam axis, the spectrum (line shape) of the registered $\gamma$ rays is given, because of the relation $E_\gamma^{Sh} = E_{\gamma_0}(1 + v_\theta/c)$, by the following formula:

$$S_{ij}(E_\gamma) = b_{ij} \int_{-\infty}^{\infty} dE_\gamma^{Sh} \Phi\left(E_\gamma, E_\gamma^{Sh}\right) \int_0^{\infty} dt\, P_\theta(t, v_\theta) \lambda_i n_i(t). \tag{1}$$

Here, $v_\theta$ is the velocity projection on the observation axis, the function $n_i(t)$ represents the time-dependent population of the level $i$, $\lambda_i$ is its decay constant, and $b_{ij}$ is the branching of the deexciting transition $i \rightarrow j$. The observed $\gamma$-ray spectrum is obtained by a convolution (folding) with the detector response function $\Phi$. The time-velocity correlations are expressed by the stopping matrix $P_\theta(t, v_\theta)$, which represents the normalized distributions of the velocity projection $v_\theta$ at different times $t$. Depending on the experimental situation, additional corrections for geometry, efficiency, angular correlation, and kinematic effects (cf. Ref. [24]) have also to be taken into account in Eq. (1). The reproduction of the line shape and the lifetime are based on solving Eq. (1) with respect to the decay function $\lambda_i n_i(t)$ of the level of interest $i$ with a correct description of the stopping process by $P_\theta(t, v_\theta)$. In addition, the influence of the feeding (i.e., of the cascade history) has also to be taken into account, indeed.

For the description of the slowdown process via Monte Carlo methods [i.e., for the calculation of the matrix $P_\theta(t, v_\theta)$], we used a modified version of the computer code DESASTOP [25,26] by Winter (cf. also Ref. [27]). The kinematics of the reactions used were also taken into account in the Monte Carlo simulation. The electronic stopping power for $^{30,32}$S ions in Si and Ta was interpolated using the semiempirical tables

of Northcliffe and Schilling [28] and corrected to take into account atomic structure effects [29,30]. The nuclear stopping power, which is due to the interaction with the atoms of the medium as a whole, was taken into account according to the Lindhard, Scharff, and Schiott (LSS) theory [31] and the parametrization of the universal scattering function for a Thomas-Fermi potential given in Ref. [32]. To correct for the effect of microchanneling in the stopping medium, the nuclear stopping power was reduced by a factor $f_n = 0.7$ (cf. Refs. [30,33] for more details).

The line shapes of the transitions to be analyzed according to the singles-like procedure were obtained:

(i) using the total singles projections of the $\gamma$-ray spectra for $^{30}$S

(ii) using the coincidence matrices by setting a gate on the full line shape of the $2_1^+ \rightarrow 0_1^+$ transition in $^{32}$S (i.e., including both its unshifted and Doppler-shifted components).

Further, for the line-shape analysis, the natural time-dependent functional form of the population $n_i(t)$ of the investigated level was used, namely,

$$n_i(t) = \sum_{k \geqslant i} C_{ik} \exp(-\lambda_k t), \tag{2}$$

which represents a superposition of exponentials with coefficients $C_{ik}$ determined by the decay constants $\lambda_k$ of the levels participating in the cascade and by the branching ratios at every level. This function is simply the solution of the Bateman equations for a system of decaying interconnected levels in cascade. Well-known recursive formulas exist for the coefficients $C_{ik}$ starting from the last level on top of the cascade.

In the general case, a fitting procedure which aims to determine simultaneously many decay constants is hindered by the necessity to find a multiparameter solution, including some parameters describing additionally the level scheme and the nonobserved or side feeding. In the present two experiments, however, performed at beam energies close to the Coulomb barrier, it was established for all levels depopulated by Doppler-shifted transitions that their observed discrete feeding can be easily identified if any. No levels above 6 MeV were populated and thus $\gamma$-$\gamma$ coincidences in two-step cascades were used for the analysis for the states above the $2_1^+$ in $^{32}$S, with a gate from below (GFB) to purify the spectra. In the case of $^{30}$S, singles line shapes were used for the investigation of the lifetimes of the $2_2^+$ and $2_1^+$ levels, but with taking into account the population patterns in the corresponding reaction and the properties of the higher lying levels, if necessary (the $2_1^+$ level case). Thereby, efficiency corrections were employed involving all detectors of Horus (we remember that there are six additional detectors at 90 deg apart from the ones displaying Doppler shifts at forward and backward angles [22]). For the $2_1^+$ level in $^{32}$S, gates were set on the shifted components of three direct feeders (GFA), thus completely eliminating the side-feeding problem. The corresponding data analysis procedure is presented in the following subsection.

### B. Analysis with gates from above (GFA)

As already mentioned, for every investigated line shape corresponding to a $\gamma$-ray depopulating the level of interest, the last two factors are correlated, i.e., the slowdown history of the ion and the time evolution of the population of the level are coupled. To illustrate how this mechanism works in a $\gamma$-$\gamma$ coincidence measurement, let us consider a hypothetical level scheme presented consisting of the levels $a$ and $b$ (the latter on top) The transitions $A$ and $B$ depopulating levels $a$ and $b$, correspondingly, are registered by two detectors, e.g., belonging to a multidetector setup (the detectors are also labeled by $A$ and $B$). Different gates can be set on the shifted portion of transition $B$. The line shape corresponding to the transition $A$ has to be analyzed. This line shape is obtained by folding the spectrum of the shifted energies $E_A^{Sh}$ [i.e., the spectrum of the velocity projections $r(v_A)$] with the detector response function $\Phi(E_A, E_A^{Sh})$. The latter function describes the probability for measuring in the full-energy peak an energy $E_A$ at incident $\gamma$-ray energy $E_A^{Sh}$. Since the gate is set on a folded spectrum, different energies $E_B^{Sh}$, respectively, different projections $v_B$, contribute to the generation of the gated spectrum. The probability to contribute, i.e., the unfolded weight, is

$$W_B(v_B) = \int_{E_B^{\min}}^{E_B^{\max}} dE_B \Phi_B\left[E_B, E_B^{sh}(v_B)\right], \tag{3}$$

where $E_B^{\min}$ and $E_B^{\max}$ indicate the lower and upper gate limits, correspondingly. Under these conditions, the spectrum of the velocity projections $r(v_A)$ for a particular slowdown (velocity) history is given by

$$r(v_A) = b_{af} \int_0^{\infty} dt_a \int_0^{t_a} dt_b W_B\left[v_B^{\kappa}(t_b)\right] \delta\left(v_A, v_A^{\kappa}(t_a)\right) \times \lambda_a \lambda_b n_b(t_b) e^{-\lambda_a (t_a - t_b)}. \tag{4}$$

In Eq. (4), $\kappa$ labels the velocity history, $b_{af}$ is the branching ratio of the transition $A$ ($a \rightarrow f$), while $\lambda_a$ and $\lambda_b$ are the decay constants of the two levels. The $\delta$ function serves to increment the content of the point in the velocity spectrum with a coordinate $v_A$ which corresponds to the projection of the ion velocity at the emission time $t_a$ of the transition $A$. The feeding transition $B$ occurs at $t = t_b$ and $W_B[v_B^{\kappa}(t_b)]$ is the unfolding weight of the velocity projection $v_B^{\kappa}(t_b)$ on the axis of the detector registering the transition $B$ at its emission time. As discussed in Ref. [34], the two-dimensional time plane ($t_a$, $t_b$) can be divided into three regions depending on the motion status of the excited nucleus at the moments of emission of the transitions $A$ and $B$:

(i) Both emissions occur during the slowdown (SS,SS),

(ii) transition $B$ occurs in slowdown (SS), $A$ occurs at rest (U), i.e., (SS,U),

(iii) both transitions occur at rest (U,U).

By setting a gate only on the shifted component of $B$, the (U,U) contribution is removed. It is possible to show that the lifetime $\tau_a$ of the level $a$ can be determined via the following formula:

$$\tau_a = \{B_{SS}, A_U\}/(d\{B_{SS}, A_{SS}\}/dt_s), \tag{5}$$

where the quantities in brackets are coincident areas and $t_s$ is the time when the nucleus comes to rest. In practice, the area of {SS,U} component can be fitted with the response function of the detector (normally a Gaussian) while the

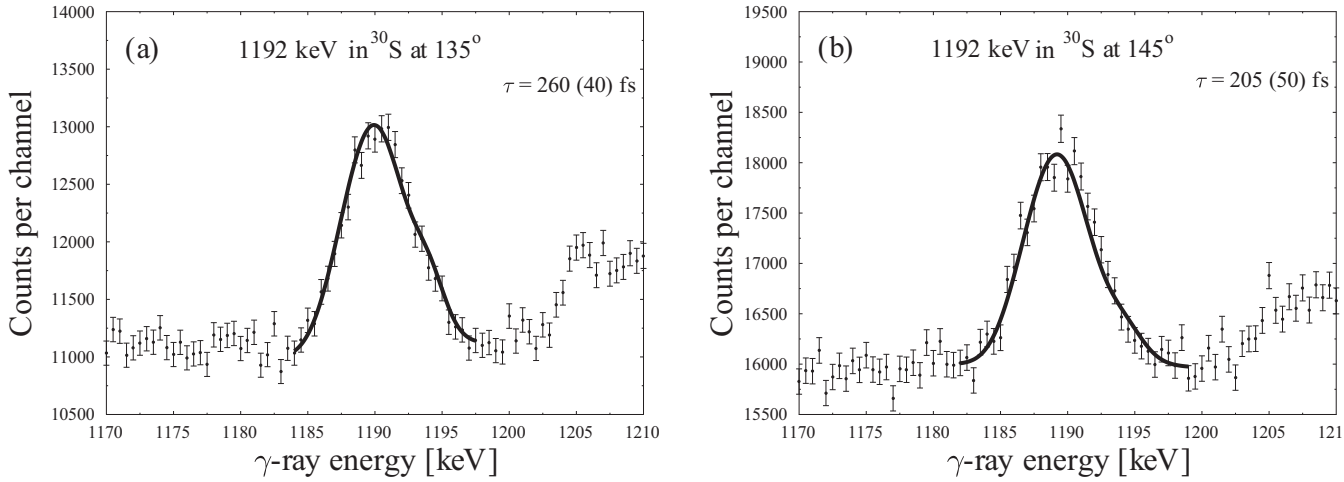


FIG. 2. Line shape analysis of the $2_2^+ \rightarrow 2_1^+$ transition in $^{30}$S at backward angles indicated in the two panels. See also text.

{SS,SS} component can be fitted using the corresponding term in Eq. (4). More details about the latter point can be found in Ref. [34]. Here we only shortly present the procedure of fitting both the line shape and the decay function $\lambda_a n_a(t)$ using second-order polynomials smoothly interconnected at a varying set of borders on the time scale. For every new set of borders, a summation over all Monte Carlo histories of the simulation is performed to generate the quantities necessary for the reproduction of the spectrum and calculation of the derivative in the denominator of Eq. (5). An important point is the necessity to know (have an initial guess for) the lifetime $\tau_a$ of the level of interest and of the decay function $\lambda_b n_b(t)$ of the feeding level. The latter can be expressed using the equation of Bateman:

$$\lambda_b n_b(t) = \lambda_a n_a(t) + \frac{dn_a(t)}{dt}. \quad (6)$$

Thus, an initial guess for the value of $\tau_a$ enters as an additional parameter in the fitting procedure. However, this value must be the same as the value deduced from the equation for the derivation of the lifetime [Eq. (5)]. Hence, the internal consistency of the procedure is not hindered by the necessity to involve a "guessed" value for $\tau_a$ as a parameter.

### C. Results for $^{30}$S

In Fig. 2, two fits of the line shapes of the $2_2^+ \rightarrow 2_1^+$ $\gamma$-ray transition of 1192 keV are displayed for the backward detector rings of Horus. At forward angles, such analysis was not possible due to the contaminating neutron-induced bump in the spectrum starting at about 1200 keV. As discussed in the section dedicated to the experiments (see also Fig. 1), the $\gamma$-$\gamma$ coincidence data confirm that the feeding of the level of interest is predominatly direct. Therefore, a single-exponential decay was employed for the description of the time evolution of the population of that state. The lifetimes derived at the angles of 135 and 145 deg are in reasonable agreement. The averaging yields a mean value of $\tau = 239$ fs with a statistical uncertainty of 31 fs. This value is larger than the adopted $\tau = 157\,(17)$ fs in the NNDC database [20]. The reasons for this discrepancy are discussed below, within the presentation of the results for the $2_1^+$ level and in Sec. III E.

In Fig. 3, fits of the line shapes of the $2_1^+ \rightarrow 0_1^+$ $\gamma$-ray transition are displayed for the four detector rings (four different polar angles with respect to the beam axis) of Horus. As already mentioned, in $^{30}$S the population of the $2_1^+$ level of interest consists of direct population and feeding from four identified higher lying states which all are direct feeders. Therefore, in order to perform the fitting procedure, it was necessary to fix the parameters of the cascades (initial population, lifetimes of the feeding level), leading to the $2_1^+$ level. The lifetime of the $2_2^+$ level was taken as determined in the present work and for the rest of the feeders the lifetimes from Ref. [20] were used. The initial populations were obtained in two steps. First, using a careful efficiency calibration and singles $\gamma$-ray spectra, the relative intensities of the 2211- and 1192-keV transitions were determined. Then, using spectra gated on the 2211-keV transition, the relative intensity of the 1192-keV transition was compared to the intensities of the other three feeding transitions (see also Fig. 1). The final data on the initial populations are presented in Table I. Thereby, the branchings in the case of more than one depopulating transitions are taken into account

Then, after fixing the background subtraction, the total peak area, and the parameters of the spectrum as FWHM, the only unknown quantity was the lifetime of the level itself. It was determined by a $\chi^2$ minimization procedure yielding also the associated uncertainties toward larger and smaller values, The final weighted average result is $\tau = 355\,(30)$ fs (the uncertainty increases to 37 fs when the systematic error due to the incomplete knowledge of the stopping powers is taken into account; see below). This lifetime value is significantly longer (more than 50%) than the value adopted in the NNDC data base of 225 (13) fs. Of course, this fact has, as discussed below, huge consequences on the systematics of the quadrupole collectivity in the even-even S isotopes which kept for long a puzzling character.

At this stage, we are not completely aware of the reasons for the discrepancies with the previous results for the lifetime of the $2_1^+$ state in $^{30}$S. However, by applying the Blaugrund

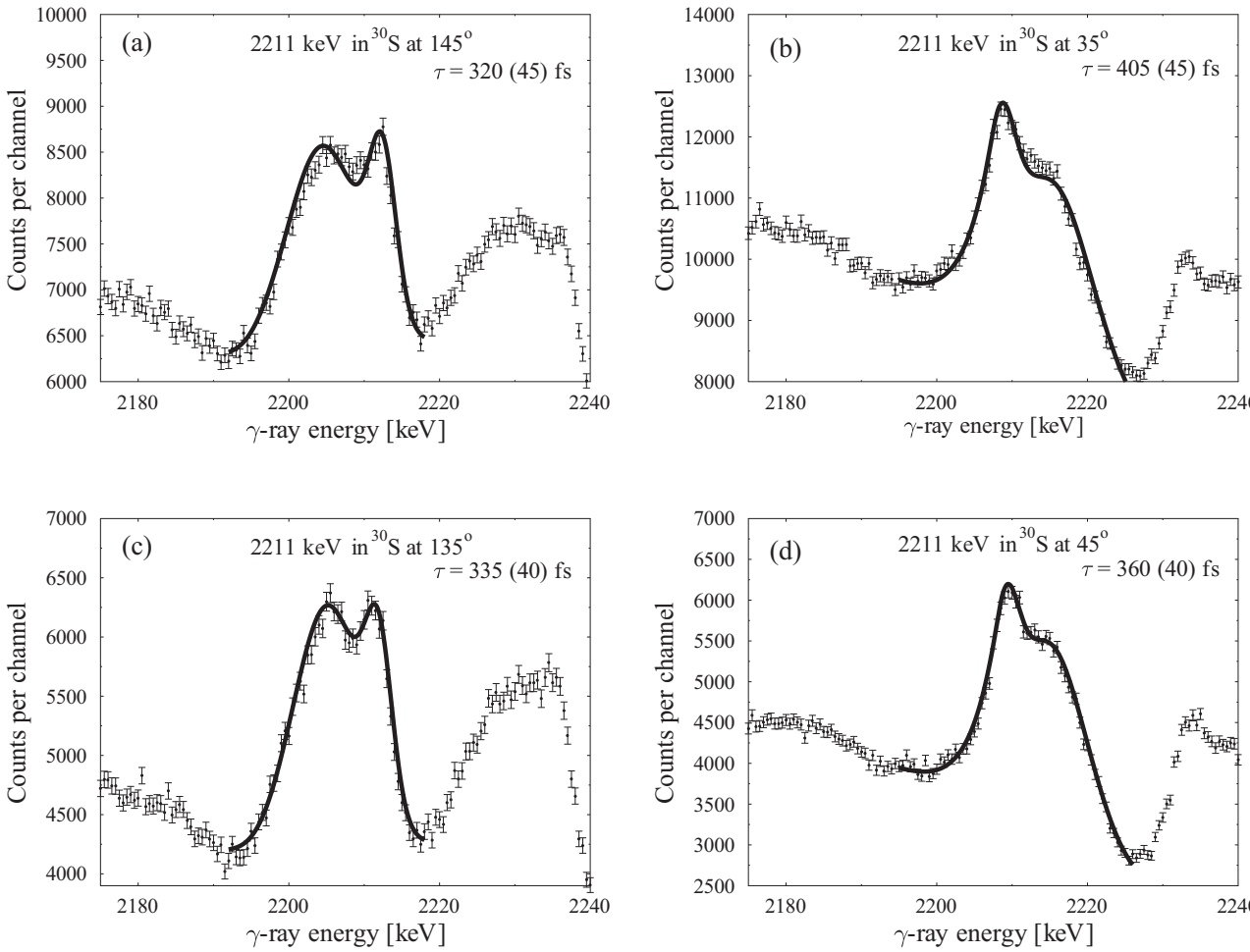


FIG. 3. Line-shape analysis of the $2_1^+ \rightarrow 0_1^+$ transition in $^{30}$S at four different observation angles [indicated in panels (a)–(d)] with respect to the beam axis. See also text.

approximation [35] for the description of the ion deceleration process as most of the previous authors from the 1970s did, we obtained immediately a strong reduction of the lifetime. The global parameters of the calculation such as stopping powers, reaction kinematics, detection of the $\gamma$ rays, etc., were thereby not changed. Simultaneously, the quality of the fit did not significantly deteriorate. This situation is further discussed and illustrated in Sec. III E. Therefore, we suggest that the differences in the description of the stopping process by the Blaugrund approximation and the Monte Carlo methods are the main reason for the disagreement with the old data with respect to the lifetime $\tau$ derived in this work. We remind that the first Monte Carlo procedure [32] was published only in 1969 and it is not completely clear how much time since then was needed to implement it in practically useful computer codes as, e.g., that of Winter [25]. However, additional factors as differences in the stopping powers used and eventually imprecise treatment of the feeding from higher lying states may also contribute somewhat to the discrepancy.

TABLE I. Relative intitial (at $t = 0$ ) population in arbitrary units of the levels observed in $^{30}$S in the present work. See also text.

| Level energy [keV] | 2211 | 3403 | 3667 | 3676 | 5136 |
|---|---|---|---|---|---|
| Spin/parity | $2_1^+$ | $2_2^+$ | | $(1^+)$ | $(3^+)$ |
| Initial population [a.u] | 100(2) | 33(3) | 6(2) | 3(1) | 8(3) |

A special comment is required to address the deviation of our result from a result for $\tau(2_1^+) = 221\,(19)$ fs obtained indirectly by a Coulomb excitation experiment at intermediate energies in Ref. [36]. The main aim of that experiment was the determination of transition strengths in $^{32}$Ar and $^{32}$Si. In this pioneering and difficult study, the authors relied on the previous mean DSAM result for the $2_1^+$ lifetime in $^{30}$S to fine-tune their analysis. In addition, the description of their setup [36] with some phoswich detectors at 0 deg indicates that the data analysis may systematically overestimate the $B(E2; 0_1^+ \rightarrow 2_1^+)$ transitions strengths and therefore underestimate the associated lifetimes. This problem is related to the very strong increase of the Rutherford cross section at 0 deg which has to be disentangled from the pure Coulomb excitation.

### D. Results for $^{32}$S

In the case of $^{32}$S, both singles-like and GFA analyses were applied, the latter only for the $2_1^+$ level. This is illustrated

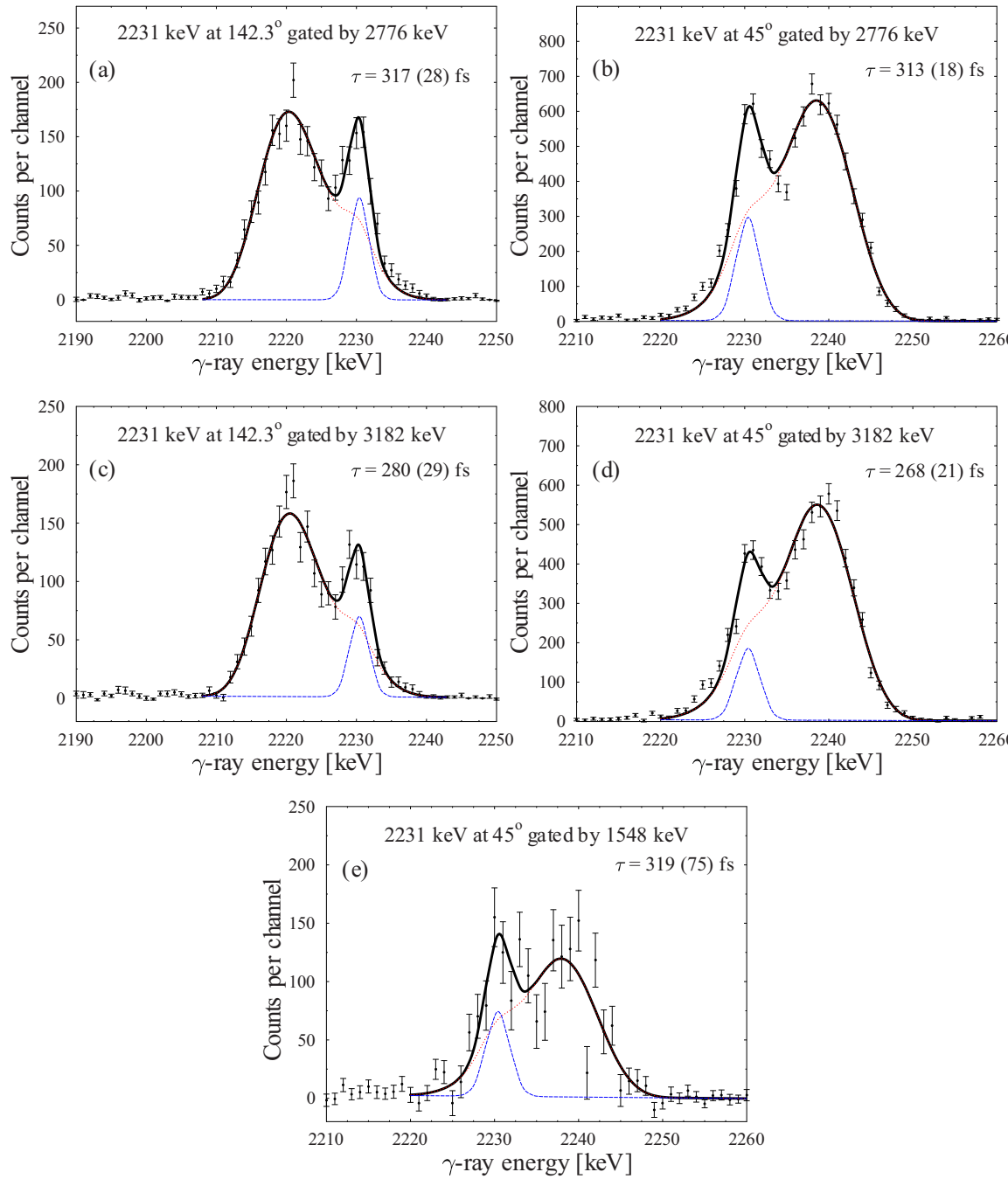


FIG. 4. Line-shape analysis and determination of the lifetime of the $2_1{}^+$ level in $^{32}$S within the GFA procedure with gates set on the shifted components of three direct feeders: [(a), (b)] the 2776-keV transition depopulating the $I^\pi = 3^-$ lying at 5006 keV; [(c), (d)] the 3182-keV transition depopulating the $I^\pi = 3^+$ lying at 5412 keV; and (e) the 1548-keV transition depopulating the $I^\pi = 0^+$ lying at 3778 keV. The decomposition of the full line shape of the gated transition into shifted and unshifted components is shown and the derived lifetime for each case is indicated. The width of the energy channel is 1 keV. See also text.

in Fig. 4 by five fits leading to quite similar values for the lifetime of the $2_1{}^+$ level. Every row of panels corresponds to a gate set on a specific direct feeder, in all three rings with the gated spectra summed up to increase statistics. The positions of the gating channels were scaled depending on the observation angle to ensure the use of the same physical events detected by every two-ring combination involved.

Higher lying levels were investigated by using the two-step cascades in which transitions depopulating them feed the $2_1{}^+$ level. Thus, their line shapes were obtained by setting a gate on the full line shape of the $2_1{}^+ \rightarrow 0_1{}^+$ $\gamma$-ray transition. These line shapes were fitted using a single exponential function representing the time dependence of the population of the levels. Only direct and no substantial cascade feeding

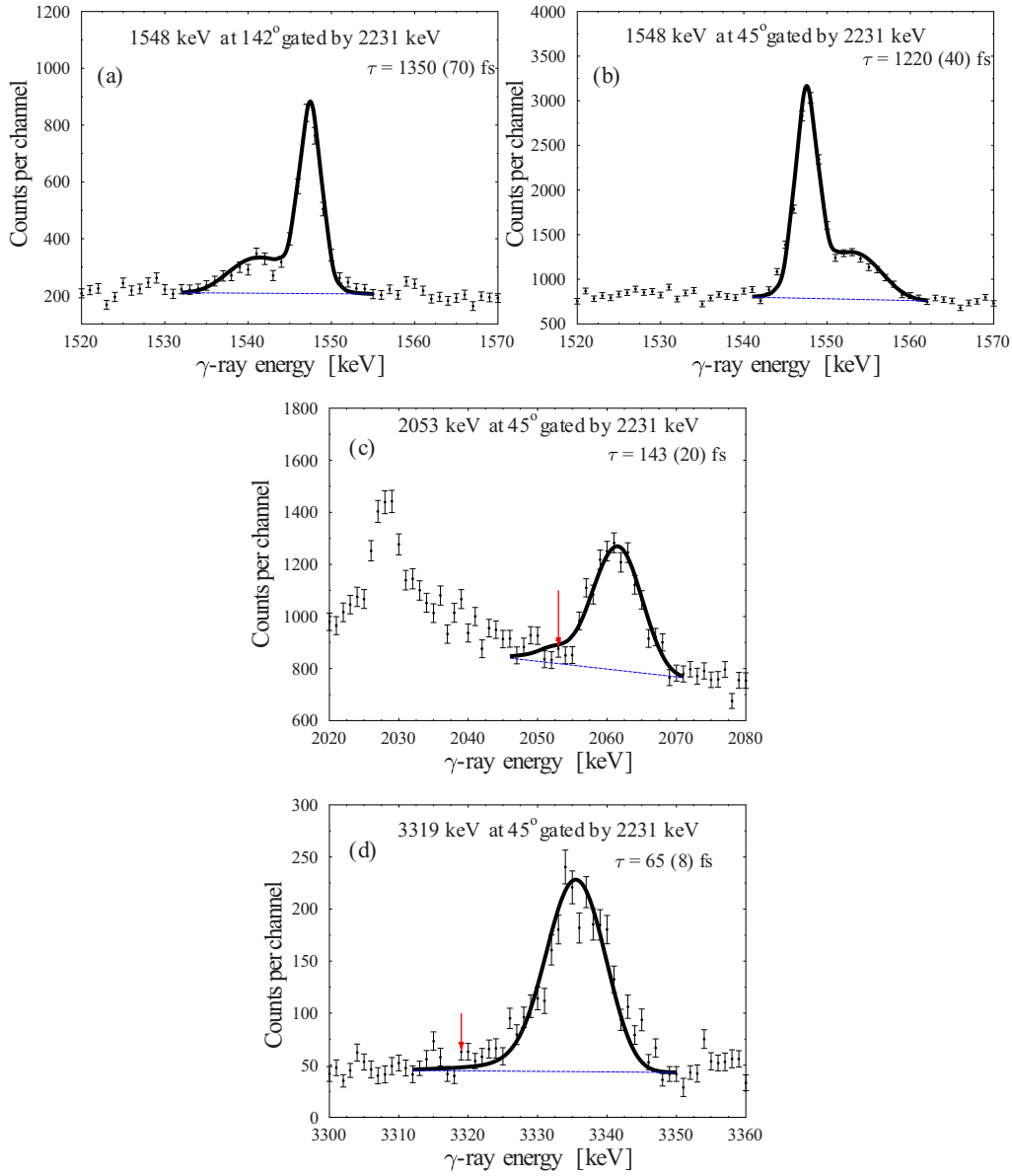


FIG. 5. Line-shape analysis ("singles-like") for three levels in $^{32}$S using spectra gated on the full line shape of the $2_1^+ \rightarrow 0_1^+$ transition: [(a), (b)] $I^\pi = 0_2^+$ level at 3778 keV depopulated by the 1548-keV transition; (c) $I^\pi = 2_2^+$ level at 4282 keV depopulated by the 2053-keV transition; (d) $I^\pi = 2_3^+$ level at 5549 keV depopulated by the 3319-keV transition. Red arrows indicate the positions of the unshifted energies (emissions at rest) of the transitions in panels (c) and (d). Note the obvious change in the line shapes of these nearly completely shifted transitions when going from the $2_2^+$ case to the $2_3^+$ one. The $2_3^+$ level has about twice shorter lifetime, indeed.

was established for them on the basis of the observed $\gamma$-$\gamma$ coincidences. This procedure is illustrated in Fig. 5 for the $0_2^+$, $2_2^+$, and $2_3^+$ states.

The result for the $2_1^+$ lifetime of $\tau = 296\,(15)$ fs requires further discussion, emphasizing the comparison with previous findings. This is achieved in Fig. 6 where the previous data are shown together with the result from the present work (here to the statistical error of 15 fs; the 6% systematic error related to the incomplete knowledge of the stopping powers, see next section, is added in quadrature to yield finally $\tau = 296\,(24)$ fs). Four methods were used in the past: DSAM, nuclear resonance fluorescence (NRF), $(e,e')$, and Coulomb excitation, the latter three methods being indirect. It is easy to see that the DSAM results (works [37] and [41]) which deviate most from our value were obtained within the Blaugrund approximation while work [38] is a private communication from the 1960s. Only one of the rest of the $\tau$ values (the NRF work [42]) does not agree with our value within the error bars, but it does on the 2-$\sigma$ level. This makes us confident that our result is reliable and precise, taking advantage of the development of the DSAM technique in coincidence mode.

The other case of disagreement with the literature is the $2_2^+$ level, which most probably can be explained by the use of the Blaugrund approximation in the past. In addition, a simple

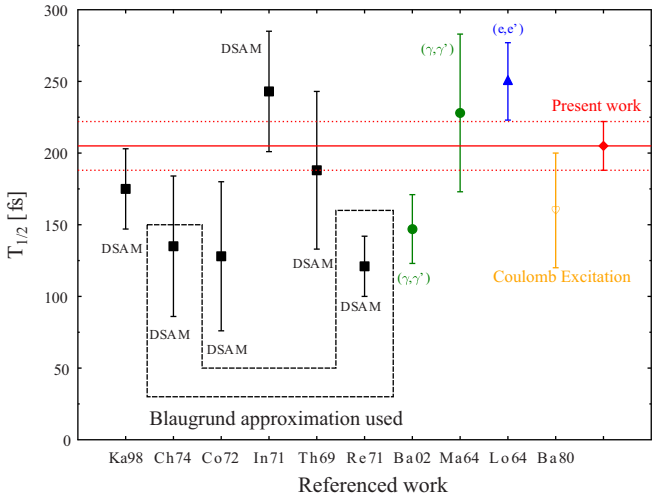


FIG. 6. Systematics of results available in the literature and from the present work on the lifetime of the $2_1{}^+$ level in $^{32}$S. Labels indicate the direct or indirect method used for the lifetime determination. The literature sources used are as follows: Ka98 [18], Ch74 [37], Co72 [38], In71 [39], Th69 [40], Re71 [41], Ba02 [42], Ma64 [43], Lo64 [44], and Ba80 [45].

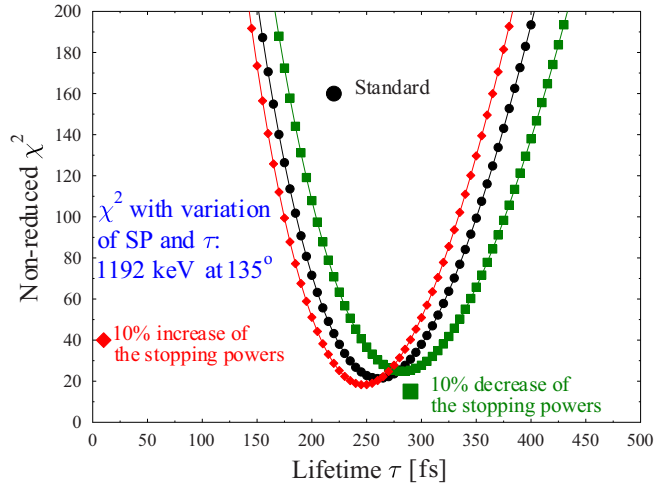


FIG. 7. Analysis of the effect of varying the electronic stopping powers on the lifetime derived. Three $\chi^2$ curves characterizing the quality of the line-shape analysis are shown. The one represented by filled circles corresponds to the set of standard stopping powers. The curve represented by diamonds corresponds to a 10% increase of the stopping powers, leading to faster deceleration and a shorter lifetime. In the case of 10% decrease (the squares), the opposite effect is observed and lifetime becomes longer. See also text.

inspection of Fig. 5 reveals that the transition depopulating the $2_3{}^+$ level is faster, and not the inverse as suggested by the values adopted in Ref. [17].

### E. Additional sources of uncertainties in the lifetimes determined

In the considerations above, the uncertainties associated with the lifetimes determined as presented in Figs. 2–5 are only of statistical character. They were obtained using error propagation including covariances of fitted parameters and $\chi^2$ analysis in a standard way. However, sources of systematic errors have to be also considered because they can significantly influence the absolute precision of the lifetimes derived.

The most important source of systematic uncertainties in DSAM is the incomplete knowledge of the stopping powers as well as the relation between the real process, leading to the deceleration of the energetic ions in material medium and the model and method used for its description in the data analysis. Also, a computer code implementing the same model and method can yield different results at variation of the stopping powers, both electronic and nuclear. Below, we concentrate exclusively on the effect of variation of the electronic stopping powers on the lifetimes derived. This effect is illustrated in Fig. 7 by three $\chi^2$ curves displayed as function of the lifetime $\tau$ of the $2_2{}^+$ level at 3403 keV in $^{30}$S. Each curve is representative for the quality of the line-shape analysis performed with three sets of electron-stopping powers. Apart the standard set (the results presented in the previous sections were obtained with them), shown are also $\chi^2$ curves obtained with a typical 10% reduction or increase of the stopping powers which normally characterizes the uncertainties of the latter. The calculations were performed for the line shape of the 1192-keV transition displayed in Fig. 2(a). On the basis of the shifts of the minima of the $\chi^2$ curves from the standard (central) position, one may conclude that the systematic uncertainty due to the incomplete knowledge of the electronic stopping powers is 10–15 fs in both directions of increase and decrease for this lifetime of 260 fs. Therefore, we estimate the relative systematic error induced by this incomplete knowledge to 6%, and correspondingly, in the final results presented below the uncertainty will include in quadrature this error.

In the following, we will illustrate the effect of the use of an inadequate model or method for the description of the slowdown, which may lead to a very large systematic error. The line-shape analysis of the 1192-kev $\gamma$-ray transition in $^{30}$S presented in Fig. 2(a) with our standard Monte Carlo simulation of the latter process, which leads to a lifetime $\tau = 260\,(40)$ fs. However, the codes originally written by Winter dispose of the option for an easy switch to the Blaugrund approximation for the description of the slowdown process. The result is shown in Fig. 8. It should be mentioned that no input parameters or stopping powers were modified before applying that option. As easily seen, a description of the line shape which is fully comparable to that shown in Fig. 2(a) is provided but the $\chi^2$ analysis leads to a very different lifetime ($\tau = 140\,(15)$ fs). Thus, using the Blaugrund approximation leads in this case to a 46% shorter lifetime. The earlier literature value is 157 (17) fs, which was derived using the Blaugrund approximation. This makes us confident of the reliability and precision of the methods employed by us in the present work and clearly indicates the main reason for disagreements with earlier DSAM studies.

A somewhat more mathematical explanation of this picture can be given by considering Eq. (1). It can be treated as an integral equation with respect to the decay function $\lambda_i n_i(t)$,

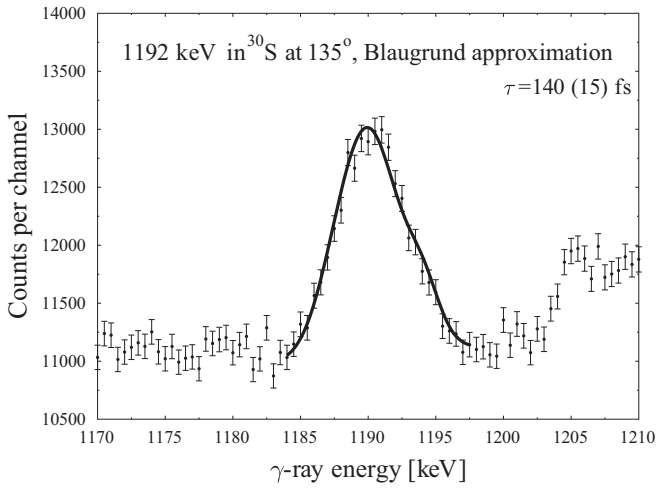


FIG. 8. Line-shape analysis of the $2_2^+ \rightarrow 2_1^+$ transition in $^{30}$S performed with a stopping matrix $P_\theta(t, v_\theta)$ [cf. Eq. (1)] calculated within the Blaugrund approximation [35]. The lifetime is derived via a $\chi^2$ analysis. Other parameters are kept fixed as in the standard calculation. Compare with Fig. 2 and see also text.

with a kernel represented by the stopping matrix $P_\theta(t, v_\theta)$. A wrong or too simplistic kernel leads to a wrong solution for the decay function.

### F. Results on lifetimes and reduced transition probabilities

The final values of the lifetimes determined in $^{30,32}$S are presented in Table II, where they are compared to previous data and displayed together with the extracted experimental $B(E2)$ [and eventually $B(M1)$] transition strengths.

In $^{32}$S, the differences between our results and earlier data are much smaller compared than in the case of $^{30}$S. The bigger discrepancy in $^{32}$S concerns the lifetime of the $2_2^+$ state. The reasons for this were discussed above. Here we would like to point out the significant difference between the properties of the $2_2^+ \rightarrow 2_1^+$ transition in the two nuclei of interest. One problem here is that the mixing ratio $\delta$ is not known in $^{30}$S, but even without this information from the inspection of Table II it is clear that relative strengths of the $E2$ and $M1$ components are very different in $^{30}$S and $^{32}$S. This empirical finding supports the general idea of the present work, that in $^{32}$S there is a local particularity of the structure of the $0_2^+$ and $2_2^+$ levels.

## IV. DISCUSSION

### A. Large size clustering

This lack of quadrupole collectivity in the shell-model and mp-mh configuration mixing calculations makes it necessary to investigate additional possible sources of the former. One option is the clustering of the constituent protons and neutrons within large agglomerations. The simplest clustering would be the formation of two slightly distant in space $^{16}$O clusters (spheres). Here we investigate the impact of such clustering on the quadrupole properties of the lower-lying $0^+$ and $2^+$ states. In the 1980s, a similar picture was suggested in terms of formation of nuclear molecules and their effect on the properties of nuclear reactions, shape isomers, and the giant quadrupole resonance (GQR) (see, e.g., Ref. [46] and references therein). However, here we will concentrate only on the simplest low-energy collective excitations in the even-even $^{32}$S close to the ground state.

In Fig. 9, the idea of the two $^{16}$O clusters is illustrated geometrically as two spheres with equal radii which partly overlap and whose centers lie on the line representing the symmetry axis of the whole $^{32}$S nucleus while the distance between the centers is $2d$. It is easy to show that the intrinsic

TABLE II. Lifetimes of levels in $^{30,32}$S derived in the present work. The energy and the spin parity of the corresponding level are shown in columns 2 and 3, respectively. The energy of the $\gamma$-ray transitions depopulating the level is displayed in column 4, followed by the determined value of the lifetime $\tau$. The multipolarity of the transition is presented in the next column. In columns 7 and 8, the reduced electromagnetic transition strengths are given in $e^2\,\mathrm{b}^2$ ($\mu_N^2$) and in Weisskopf units, respectively. In the last column, the adopted lifetimes in the NNDC [17,20] prior to the present work are given. Spectroscopic data necessary for the calculation of the transition probabilities were taken also from Refs. [17,20].

| Nucleus | $E_{\mathrm{lev}}$ [keV] | $I^\pi$ | $E_\gamma$ [keV] | $\tau$ [fs] | $\sigma\lambda$ | B($\sigma\lambda$) [$e^2\,\mathrm{b}^2/\mu_N^2$] | B($\sigma\lambda$) [W.u.] | $\tau_{\mathrm{Literature}}$ [fs] |
|---|---|---|---|---|---|---|---|---|
| $^{30}$S | 2210.6 | $2_1^+$ | 2210.6 | 355 (37) | $E2$ | $4.36(46) \times 10^{-3}$ | 7.9 (8) | 225 (13) |
| | 3402.6 | $2_2^+$ | 1192.0 | 239 (35) | Assumed $\delta = 1$ | $E2 : 5.7(9) \times 10^{-2}$ | 103 (15) | 157(17) |
| | | | | | | $M1 : 5.6(8) \times 10^{-2}$ | $3.1(5) \times 10^{-5}$ | |
| | | | 3402.6 | | $E2$ | $1.5(3) \times 10^{-4}$ | 0.27(5) | |
| $^{32}$S | 2230.6 | $2_1^+$ | 2230.6 | 296 (23) | $E2$ | $5.0(4) \times 10^{-3}$ | 8.3 (7) | 244 (16) |
| | 3778.4 | $0_2^+$ | 1548.8 | 1260 (91) | $E2$ | $7.3(6) \times 10^{-3}$ | 12.0 (9) | 1284 (130) |
| | 4281.8 | $2_2^+$ | 2052.6 | 142 (15) | $\delta = -26(16)$ | $E2 : 1.1(3) \times 10^{-3}$ | 1.8 (5) | 61(6) |
| | | | | | | $M1 : 4.8(6) \times 10^{-5}$ | $2.7(3) \times 10^{-5}$ | |
| | | | 4281.5 | | $E2$ | $3.7(4) \times 10^{-4}$ | 0.62(8) | |
| | 5548.5 | $2_3^+$ | 3318.5 | 65 (9) | $\delta = -5.2\,(2.1)$ | $E2 : 1.8(3) \times 10^{-3}$ | 3.0 (4) | 82 (12) |
| | | | | | | $M1 : 5.1(4.0) \times 10^{-4}$ | $2.9(2.3) \times 10^{-4}$ | |
| | | | 5546.4 | | $E2$ | $9.6(1.3) \times 10^{-5}$ | 0.16 (2) | |

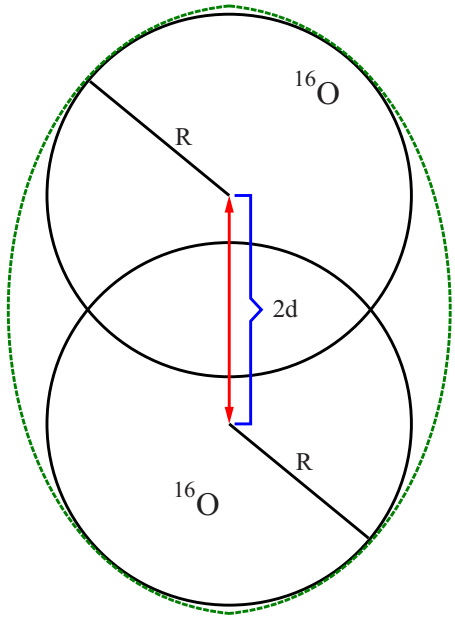


FIG. 9. Geometrical sketch of the two $^{16}$O cluster configuration in $^{32}$S.

quadrupole moment of this system can be expressed as

$$Q_0 = -\frac{2Z\pi}{5}\frac{\left(\frac{135}{12}d^5 - 15d^3R^2 - \frac{20}{3}d^2R^3 + \frac{5}{2}dR^4\right)}{\frac{4\pi}{3}\left(R^3 + \frac{3}{2}dR^2 - \frac{1}{2}d^3\right)}. \quad (7)$$

In principle, both rigid deformation and/or vibrations may be responsible for the establishment of a mean distance $2d$ between the two spheres. Based on the formulas of the rigid rotor model [47] and Eq. (7), we calculate in the following the reduced matrix elements for the $E2$ transitions and quadrupole moments associated with states belonging to a class we call "cluster states." A successful reproduction of the experimental data leads obviously to the determination of $Q_0$ and therefore of $d$, the parameter describing geometrically the large-size clustering in $^{32}$S in its simplest version.

### B. Two-band mixing calculation for $^{32}$S

Of course, it would be too simple and unrealistic to involve only the cluster states when trying to reproduce the experimental data related to the quadrupole collectivity. Therefore, let us consider separately a two-level mixing for the lowest experimental two $0^+$ and two $2^+$ levels in $^{32}$S. The ingredients of the mixing belong, on the one hand, to the shell-model space (abbreviation index "sh") and, on the other hand, to the deformed (statically or dynamically) two-cluster space (abbreviation index "cl"). A given interaction strength $V_I$ between the unperturbed states determines uniquely the mixing amplitudes for each spin I since the experimental level energies are known. The low-lying states in $^{32}$S and the experimental data available on the quadrupole properties are shown in Fig. 10. The wave functions of the physical (perturbed) levels, which are also shown, represent a superposition of the two discussed structures (unperturbed states). Using the standard formulas for the two-level mixing case, the

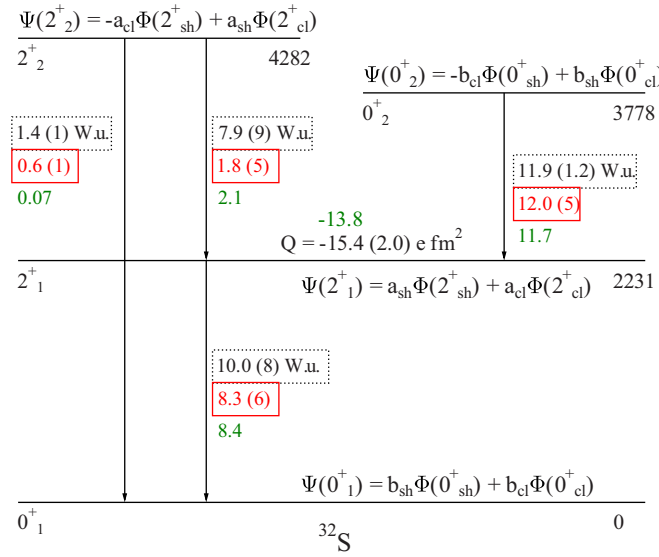


FIG. 10. The experimental energies of the low-lying $I^\pi = 0^+$ and $2^+$ states in $^{32}$S together with experimental $B(E2)$ transition strengths and the quadrupole moment of the $2_1{}^+$ level. Our new data are presented in red in framed boxes and in Weisskopf units. Previous data on the $B(E2)$'s are in framed dotted boxes and in black. The third number characterizing each transition (in green) is the result of the present two-level mixing calculation. The structure of the mixed wave functions is also indicated. The best fit to the data was obtained with the following values of the amplitudes: $b_{sh} = 0.9768$, $b_{cl} = -0.2141$, $a_{sh} = 0.9350$, and $a_{cl} = -0.3546$. See also text.

corresponding amplitudes can be calculated for every possible interaction strength $V_I$.

The intrastructure reduced $E2$ matrix elements $\langle I_f||E2||I_i\rangle$ (sh $\rightarrow$ sh, cl $\rightarrow$ cl) are either theoretically known, taken from the literature [16] (case sh), or calculated for a fixed average distance $2d$ between the two magic clusters in the latter case (see previous subsection). Here we mention that the diagonal matrix element $\langle 2||E2||2\rangle$ is proportional to the quadrupole moment of the corresponding state. Also, we used the scaled versions of the matrix elements from [16] (Fig. 6 in that work), which are fixed to reproduce the $B(E2; 2_1{}^+ \rightarrow 0_1{}^+)$ transition strength in $^{28,34}$S on both sides of the $^{30,32}$S data. In addition, the assumption that the interstructure $E2$ matrix elements are negligible in the formation of the total $E2$ transition matrix element between the perturbed states compared to the intrastructure ones was made since the nature of the mixing excitations is very different. This assumption is somewhat different from what was employed by us in Ref. [10] where the sh $\rightarrow$ cl and cl $\rightarrow$ sh matrix elements were also fitted.

A fitting procedure was carried out using a dedicated computer code and consisted of varying the interaction strengths between the unperturbed states as well as the mean distance between the centers of the two overlapping spheres representing the cluster configuration. Thereby, a minimization of $\chi^2$ built by comparing the experimental reduced transition matrix elements and the quadrupole moment of the first excited $2^+$ level with the theoretical values was performed.

TABLE III. Experimental and theoretical values of quadrupole observables in $^{32}$S. The two-level mixing calculation yields negative signs for the $\langle 0_1{}^+||E2||2_2{}^+\rangle$ and $\langle 2_1{}^+||E2||0_2{}^+\rangle$ reduced matrix elements while such signs characterize in our shell-model calculation (column 4) the $\langle 0_1{}^+||E2||2_1{}^+\rangle$ and $\langle 2_1{}^+||E2||2_1{}^+\rangle$ matrix elements.

| Quantity | Experiment [$e$ fm$^2$] | Present work: Clusters [$e$ fm$^2$] | Present work: Shell model [$e$ fm$^2$] | Shell model [18] [$e$ fm$^2$] |
|---|---|---|---|---|
| $Q(2_1^+)$ | −15.4 (2.0) [17] | −13.8 | −11.7 | |
| $\lvert\langle 0_1{}^+\|\|E2\|\|2_1{}^+\rangle\rvert$ | 15.8 (6) | 15.9 | 16.4 | 15.7 |
| $\lvert\langle 0_1{}^+\|\|E2\|\|2_2{}^+\rangle\rvert$ | 4.3 (2) | 1.5 | 7.8 | 7.8 |
| $\lvert\langle 2_1{}^+\|\|E2\|\|2_2{}^+\rangle\rvert$ | 7.4 (1.0) | 8.0 | 17.6 | 16.3 |
| $\lvert\langle 2_1{}^+\|\|E2\|\|0_2{}^+\rangle\rvert$ | 8.5 (2) | 8.4 | 7.3 | 6.7 |

The final results are presented in Table III together with additional theoretical matrix elements from one earlier work [18] and calculations performed within the present work with the shell-model code NUSHELLX@MSU [48] using the interaction USDA [49] and the systematics of effective charges in Ref. [50].

The agreement between the presently deduced values by the two-level mixing calculation and experiment is better than that provided by both shell-model calculations used for comparison. The relatively lower quality of the description of the decay of the $2_2{}^+$ level may occur due to the influence of the $2_3{}^+$ level, lying only about 1 MeV higher, and whose effect was not taken into account in the two-level mixing calculation.

As already mentioned, the ever-increasing predictive power of the shell model leads both to enlargement of the portion of the nuclear map where they give very good results and perfecting the results in earlier successfully described mass regions. Within the context of the $A \approx 30$ region, for example, in Ref. [16] the question of the weaker theoretical collectivity in $^{32}$S with reasonable (not specially normalized) effective $E2$ charges was again raised. From that point of view, our results indicate one possible solution of that problem. The missing collectivity may be at least partly provided by a mixing of the normal (shell-model states) with states associated with much more deformed nuclear shape, namely, the two-cluster states based on $2x^{16}$O configuration. Thereby, the deduced value for the half-distance parameter $d \approx 2.84$ fm correlates reasonably with the result for the radius $R(^{32}S) = 3.26$ fm from the literature [51]. A straightforward application of the standard formula for the nuclear radius $R = 1.2A^{1/3}$ fm leads to a radius of about 3.0 fm for $^{16}$O, which would mean that the two large clusters only slightly overlap when that excitation takes place. Geometrically, this configuration is characterized by an intrinsic quadrupole moment $Q_0{}^{\sim} = 104\,e$ fm, which is very large and even a small mixing may lead to a strong enhancement of the quadrupole collectivity observed at the low-lying states. An additional result of the two-level mixing calculation is the interaction strength $V_{0^+,2^+}$ between the unperturbed states. For the $0^+$ states, it is about 0.79 MeV. For the $2^+$ levels, $V \approx 0.68$ MeV. The mixing percentages amount to 4.6% at the $0^+$ states and 12.6% at the $2^+$ states. We note that the physical (perturbed) $2^+$ states are much closer to each other compared to the two $0^+$ ones.

Can a $2_2{}^+ \to 0_2{}^+$ $\gamma$-ray transition can be observed experimentally? Within the present considerations it should be characterized by very strong $B(E2)$ transition strength. It is the case, indeed, and this strength is about 52 times larger then the $B(E2; 2_2{}^+ \to 0_1{}^+)$ transition strength. However, due to the energy factor which goes as $E_\gamma^5$, the intensity of the latter transition would be about 850 times stronger and a registration of the $2_2{}^+ \to 0_2{}^+$ $\gamma$-ray transition is below the sensitivity limit of our setup.

To conclude, our new lifetime data for $^{30,32}$S and the proposed interpretation seem to minimize and maybe even solve the problem of missing theoretical collectivity in these two isotopes. On the one hand, the longer lifetimes, especially in $^{30}$S, favor the use of the shell model with conveniently chosen effective charges. On the other hand, in $^{32}$S, a weaker but still noticeable effect on the $B(E2)$'s of 20–25% remains after that use, and finds an explanation with the two $^{16}$O clusters. In the fitting procedure, we used scaled $\langle 0_{sh}{}^+||E2||2_{sh}{}^+\rangle$ and $\langle 2_{sh}{}^+||E2||2_{sh}{}^+\rangle$ matrix elements. Therefore, the role of the clusterization may be even somewhat underestimated in the results of the calculation.

Now, let us try to position this picture within the systematics and relate it to well-established microscopical findings concerning the evolution of the single-particle orbitals for $Z, N \leqslant 20$.

### C. Systematics of low-lying quadrupole states in some even-even sulfur isotopes

In Fig. 11, the experimental excitation energies of the $2_1{}^+$, $0_2{}^+$, $2_2{}^+$, and $4_1{}^+$ levels in the even-even sulfur isotopes with $A = 28$–38 are shown, when available. The $2_1{}^+$ levels are also characterized by the $B(E2)$ transition strengths to the ground state $0_1{}^+$ in Weisskopf units. The observed features may be easily associated with the evolution of the filling of the single-particle orbitals in the $N = 8$–20. We note that the number of $Z = 16$ protons is only slightly displaced from the midshell ($Z = 14$). An inspection of the Nilsson diagram with the aim to localize the active single-particle orbitals immediately relates the gross features of the systematics on Fig. 11 to the subsequent filling of the $sd$ subshells. More specifically, the subshell $1d_{5/2}$ is filled in $^{30}$S at $N = 14$ while in $^{32}$S, at $N = 16$, the $2s_{1/2}$ subshell is completely occupied by two neutrons. These effects explain the increase of the excitation energy of the $2_1{}^+$ state in $^{30,32}$S compared to $^{28}$S, while the sharper new increase at $N = 20$ is associated with magicity indeed. The behavior of the $0_2{}^+$ state is peculiar, in the sense that it comes abruptly down at $N = 16$, and its excitation energy decreases when approaching the magic number $N = 20$, in contrast to

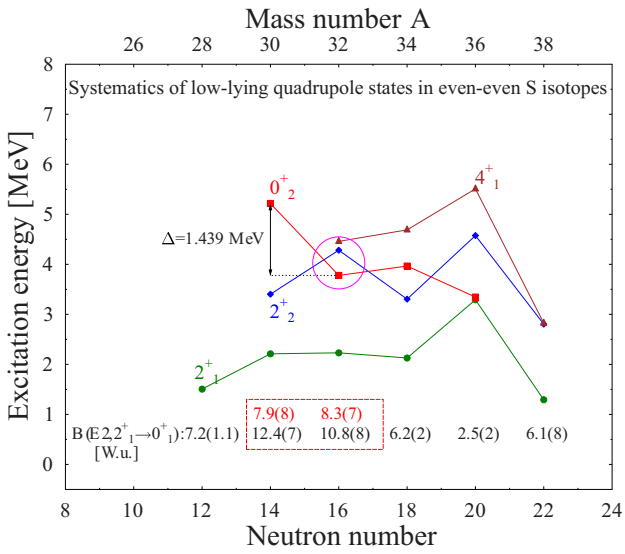


FIG. 11. Experimental level energies of some low-lying quadrupole states in a chain of S isotopes. The $B(E2; 2_1^+ \rightarrow 0_1^+)$ transition strength is also indicated in Weisskopf units for each isotope on the bottom. Our new values are in the framed box, on the upper row and in red.

all other excited states. Therefore, specific intruder features could be associated with this state in $^{32}$S, and/or it may be a realization of the large-size cluster states discussed (of course, in a not completely pure configuration). Further, in this nucleus the $I^\pi = 2_2^+$ level abruptly "jumps" above the $0_2^+$ state and thus suggests the observation of an admixed excitation on top of a bandhead represented by the $0_2^+$ state as indicated by the circle in the middle of Fig. 11. Of course, the fact that a $2_2^+ \rightarrow 0_2^+$ $\gamma$-ray $E2$ transition is not observed needs an explanation. According to the results of the two-band mixing calculation from the previous section, a $B(E2)$ value of about 35 W.u. is expected for that transition. However, the latter transition competes with the $2_2^+ \rightarrow 0_1^+$ and $2_2^+ \rightarrow 2_1^+$ transitions which are favored by the $E_\gamma^5$ energy factor about $44 \times 10^3$ and $1 \times 10^3$ times, respectively (cf. Fig. 10). Therefore, such transition is not easy to be detected experimentally.

An additional argument supporting the unique character of the $0_2^+$ state in $^{32}$S within the isotopic chain is the reduction of the $B(E2; 0_2^+ \rightarrow 2_1^+)$ strength in neighboring $^{34}$S. Namely, the corresponding value of 4.2 (7) W.u. is about 3 times smaller than the corresponding quantity in $^{32}$S (12.0 W.u).

The nuclear structure effect proposed in the present paper, namely the role of large-size clustering, seems to be appropriate for explaining the evolution of the quadrupole collectivity in the even-even sulfur isotopes around $^{32}$S. Our extremely simple phenomenological approach, however, should be verified by much deeper theoretical efforts which are far beyond the scope of the present experimental work.

### D. Further possible cases of large size clustering

Is it possible to observe similar effects in other regions of the nuclear map? In our opinion, yes, and it is possible even to establish a connection between the two $^{16}$O cluster picture in $^{32}$S and the experimental observation that the yrast band in $^{80}$Zr points to a very large quadrupole deformation associated with it [52], namely, $\beta_2 \approx 0.4$, i.e., an ellipsoid axis ratio of 3/2. This finding is based only on the level energies in the rotational yrast band [53] since no lifetime measurements were preformed so far in that nucleus, which is difficult to access via fusion-evaporation reactions ($\sigma \propto 10\,\mu$b). It should be mentioned that the nuclei with $N \approx Z$ and $A \approx 80$ are among the most deformed nuclei observed so far. In the work of Zheng and Zamick [54], the question of superdeformation in $^{80}$Zr was discussed as well the coexistence of a spherical band and a superdeformed band with an axis ratio of 2/1. The stability of that nucleus with respect to exotic (i.e., large) cluster decays was considered in Ref. [55]. In the spirit of the present work, some excitations in $^{80}$Zr may be considered to be based on a two-cluster configuration consisting of two doubly magic $^{40}$Ca nuclei. One may assume that the yrast band of $^{80}$Zr and the excitation based on the $0_2^+$ state in $^{32}$S have the same origin—large size clustering of the constituent nucleons. We mention that our two symmetric-cluster picture illustrated in Fig. 9 at $d \approx R$ corresponds roughly to longer/smaller axis ratio of 2/1 of the ellipsoid drawn schematically around the two spheres. Of course, this type of consideration might not reach the very depth of the phenomenon, e.g., with the approximation that the nuclear charge density drops to zero inside this ellipsoid, in the regions not occupied by the spheres. Much more advanced theoretical efforts are needed in order to reach eventually a quantitative quantum mechanical description.

Another example of the type considered could be $^{16}$O with its $2_2^+$ and $0_2^+$ levels at 6.917 and 6.049 MeV, respectively, interconnected by a strong $E2$ transition with $B(E2) = 27$ (3) W.u. [56]. Here, one may invoke a picture where the clusters are formed by 8 protons and 8 neutrons. Of course, the stability of these systems would be impossible outside the nucleus, but inside, they could move (e.g., vibrate) against each other. Again, a deeper insight into this picture is beyond the scope of the present paper. Nevertheless, an association with the scissors mode [57,58], which consists of the relative vibration of (axially) deformed neutron and proton fluids in heavy nuclei, makes our large-size clustering picture more plausible. In principle, one could imagine a nuclear collective motion of that type also in systems consisting of asymmetric clusters with different numbers of nucleons, associated, e.g., with specific subshell closures.

## V. CONCLUSIONS

The comparison between experimental and theoretical transition and diagonal electromagnetic matrix elements provides nuclear structure information which may become crucial in many cases. The presently suggested existence of large-scale clustering, especially the one involving magic clusters, may explain the insufficient (so far) shell-model quadrupole collectivity in some nuclei. In this way, a new type of collective motion (relative cluster displacement and/or vibrations) at relatively low excitation energy above the ground state may interfere with the standard (although not easy to describe)

mp-mh excitations. Such an effect consistently was shown to be a possible origin of the enhanced experimental quadrupole collectivity in $^{32}$S correlated to the filling of subshells, i.e., with the single-particle properties. A similar picture may be invoked for $^{80}$Zr where the experimental information available at present on quadrupole collectivity is very scarce. Experiments are planed to investigate $E2$ transition strengths in that nucleus and additional systematic phenomenological studies in other mass regions are in progress. In addition to these aspects, an experimental point arises: The quite extensive use of the Blaugrund approximation when applying DSAM in the past requires revisiting at least some key lifetime data in light nuclei to improve the precision of the input for theoretical considerations, and especially for advanced shell-model ones, in near future.

## ACKNOWLEDGMENTS

The authors are thankful to A. Astier, M.-G. Porquet, P. Schuck, and O. Yordanov for fruitful discussions. They are also grateful to the Deutsche Forschungsgemeinschaft for the support under Contract No. ZI 510/8-1.

[1] P. Ring and P. Schuck, *The Nuclear Many-Body Problem* (Springer, Berlin, 1980).
[2] F. A. Majeed, *No-Core Shell Model Calculations for Some Light Nuclei* (Scholar's Press, 2015).
[3] G. C. Bonsignori, M. Bruno, A. Ventura, and D. Vretenar, *Hadrons, Nuclei, and Applications*, Vol. 3 (World Scientific, Singapore, 2001).
[4] C. Beck, *Clusters in Nuclei*, Vol. 3 (Springer, Berlin, 2013).
[5] A. Astier, P. Petkov, M.-G. Porquet, D. S. Delion, and P. Schuck, Phys. Rev. Lett. **104**, 042701 (2010).
[6] M. Spieker, S. Pascu, A. Zilges, and F. Iachello, Phys. Rev. Lett. **114**, 192504 (2015).
[7] D. H. E. Gross, Rep. Prog. Phys. **53**, 605 (1990).
[8] R. H. Spear, Phys. Rep. **73**, 369 (1981).
[9] S. Ohkubo and K. Yamashita, Phys. Rev. C **66**, 021301 (2002).
[10] P. Petkov and M. Stoyanova, Bulg. J. Phys. **42**, 565 (2015).
[11] E. Caurier, G. Martinez-Pinedo, F. Nowacki, A. Poves, and A. P. Zuker, Rev. Mod. Phys. **77**, 427 (2005).
[12] T. Otsuka, M. Honma, T. Mizusaki, N. Shimuzo, and Y. Utsuno, Prog. Part. Nucl. Phys. **47**, 319 (2001).
[13] B. A. Brown and B. H. Wildenthal, Annu. Rev. Nucl. Sci. **38**, 29 (1988).
[14] M. Bender, P.-H. Heenen, and P.-G. Reinhard, Rev. Mod. Phys. **75**, 121 (2003).
[15] J.-P. Delaroche, M. Girod, J. Libert, H. Goutte, S. Hilaire, S. Peru, N. Pillet, and G. F. Bertsch, Phys. Rev. C **81**, 014303 (2010).
[16] J. Le Blois, N. Pillet, M. Dupuis, J. M. Daugas, L. M. Robledo, C. Robin, and V. G. Zelevinsky, Phys. Rev. C **89**, 011306(R) (2014).
[17] B. Singh, Nucl. Data Sheets **112**, 2199 (2011).
[18] A. Kangasmaki, P. Tikkanen, J. Keinonen, W. E. Ormand, S. Raman, Zs. Fülöp, A. Z. Kiss, and E. Somorjai, Phys. Rev. C **58**, 699 (1998).
[19] E. Kuhlmann, W. Albrecht, and A. Hoffmann, Nucl. Phys. A **213**, 82 (1973).
[20] B. Shamsuzzoha, Nucl. Data Sheets **111**, 2331 (2010).
[21] A. Linnemann, Ph.D. thesis, University of Cologne, Cologne, Germany, 2005 (unpublished).
[22] L. Netterdon, V. Derya, J. Endres, C. Fransen, A. Hennig, J. Mayer, C. Müller-Gatermann, A. Sauerwein, P. Scholz, M. Spieker, and A. Zilges, Nucl. Instrum. Methods Phys. Res., A **754**, 94 (2014).
[23] J. M. G. Caraça, R. D. Gill, A. J. Cox, and H. J. Rose, Nucl. Phys. A **193**, 1 (1972).
[24] T. K. Alexander and J. S. Forster, Adv. Nucl. Phys. **10**, 197 (1978).
[25] G. Winter, ZfK Rossendorf Report ZfK-497, Central Institute for Nuclear Research, Rossendorf, 1983.
[26] G. Winter, Nucl. Instrum. Methods **214**, 537 (1983).
[27] P. Petkov, J. Gableske, O. Vogel, A. Dewald, P. von Brentano, R. Krücken, R. Peusquens, N. Nicolay, A. Gizon, J. Gizon, Nucl. Phys. A **640**, 293 (1998).
[28] L. C. Northcliffe and R. F. Schilling, Nucl. Data Tables A **7**, 233 (1970).
[29] J. F. Ziegler and W. K. Chu, At. Data Nucl. Data Tables **13**, 463 (1974).
[30] J. F. Ziegler and J. P. Biersack, in *Treatise on Heavy-Ion Science*, Vol. 6, edited by D. A. Bromley (Plenum Press, New York, 1985), p. 95.
[31] J. Lindhard, M. Scharff, and H. E. Schiøtt, Mat. Fys. Medd. K. Dan. Vidensk. Selsk. **33**, 14 (1963).
[32] W. M. Currie, Nucl. Instrum. Methods **73**, 173 (1969).
[33] J. Keinonen, in *Capture Gamma-Ray Spectroscopy and Related Topics—1984*, *Proceedings of the Fifth International Symposium, Knoxville, Tennessee*, edited by S. Raman, AIP Conf. Proc. No. 125 (AIP, New York, 1985), p. 557.
[34] P. Petkov, D. Tonev, J. Gableske, A. Dewald, and P. von Brentano, Nucl. Instrum. Methods Phys. Res. A **437**, 274 (1999).
[35] A. E. Blaugrund, Nucl. Phys. **88**, 501 (1966).
[36] P. D. Cottle, Z. Hu, B. V. Pritychenko, J. A. Church, M. Fauerbach, T. Glasmacher, R. W. Ibbotson, K. W. Kemper, L. A. Riley, H. Scheit, and M. Steiner, Phys. Rev. Lett. **88**, 172502 (2002).
[37] Y. T. Cheng, A. Goswami, M. J. Throop, and D. K. McDaniels, Phys. Rev. C **9**, 1192 (1974).
[38] P. Coussement (Private communication).
[39] F. Ingebretsen, B. W. Sargent, A. J. Ferguson, J. R. Leslie, A. Henrikson, and J. H. Montague, Nucl. Phys. A **161**, 433 (1971).
[40] J. P. Thibaud, M. M. Aleonard, D. Castera, P. Hubert, F. Leccia, and P. Mennrath, Nucl. Phys. A **135**, 281 (1969).
[41] M. J. Renan and R. J. Keddy, Nuovo Cimento A **3**, 347 (1971).
[42] Y. A. Luo, J. Q. Chen, T. F. Feng, and P. Z. Ning, Phys. Rev. C **64**, 037303 (2002).
[43] D. L. Malaker, L. Schaller, and W. C. Miller, Bull. Am. Phys. Soc. **9**, AB7 (1964).
[44] R. Lombard, P. Kossanyi-Demay, and G. R. Bishop, Nucl. Phys. **59**, 398 (1964).

[45] G. C. Ball, O. Häusser, T. K. Alexander, W. G. Davies, J. S. Forster, I. V. Mitchell, J. R. Beene, D. Hörn, and W. Mclatchie, Nucl. Phys. A **349**, 271 (1980).
[46] K. Langanke, Phys. Rev. C **28**, 1574 (1983).
[47] A. Bohr and B. R. Mottelson, *Nuclear Structure*, Vol. II (Benjamin-Cummings, Reading, MA, 1975).
[48] B. A. Brown and W. D. M. Rae, Nucl. Data Sheets **120**, 115 (2014).
[49] B. A. Brown and W. A. Richter, Phys. Rev. C **74**, 034315 (2006).
[50] W. A. Richter, S. Mkhize, and B. A. Brown, Phys. Rev. C **78**, 064302 (2008).
[51] K. Marinova and I. Angeli, At. Data Nucl. Data Tables **99**, 69 (2013).
[52] C. J. Lister, M. Campbell, A. A. Chishti, W. Gelletly, L. Goettig, R. Moscrop, B. J. Varley, A. N. James, T. Morrison, H. G. Price, J. Simpson, K. Connel, and O. Skeppstedt, Phys. Rev. Lett. **59**, 1270 (1987).
[53] B. Singh, Nucl. Data Sheets **105**, 223 (2005).
[54] D. C. Zheng and L. Zamick, Phys. Lett. B **266**, 5 (1991).
[55] R. Gupta, W. Scheid, and W. Greiner, J. Phys. G **17**, 1731 (1991).
[56] J. H. Kelley, D. R. Tilley, H. R. Weller, and C. M. Cheves, Nucl. Phys. **564**, 1 (1993).
[57] D. Bohle, A. Richter, W. Steffen, A. E. L. Dieperink, N. Lo Iudice, F. Palumbo, and O. Scholten, Phys. Lett. B **137**, 27 (1984).
[58] D. Bohle, G. Kiichler, A. Richter, and W. Steffen, Phys. Lett. B **148**, 260 (1984).